Chemical Engineering Journal 480 (2024) 147740

Contents lists available at ScienceDirect

Chemical Engineering Journal

journal homepage: www.elsevier.com/locate/cej

Synthesis of persistent luminescence nanocage as both drug nanocarrier and autofluorescence-free bioimaging agent for the theranostics of bacterial infection

Xuan Fu [a,b,c], Li-Xia Yan [a,b,c], Xu Zhao [a,b,c], Li-Jian Chen [a,b,c], Xiu-Ping Yan [a,b,c,d,*]

[a] State Key Laboratory of Food Science and Resources, Jiangnan University, Wuxi 214122, China
[b] International Joint Laboratory on Food Safety, Jiangnan University, Wuxi 214122, China
[c] Institute of Analytical Food Safety, School of Food Science and Technology, Jiangnan University, Wuxi 214122, China
[d] Key Laboratory of Synthetic and Biological Colloids, Ministry of Education, Jiangnan University, Wuxi 214122, China

ARTICLE INFO

Keywords:
Persistent luminescence
Mesoporous materials
Drug delivery
Antibacterial therapy
Bioimaging

ABSTRACT

Persistent luminescent nanoparticles (PLNPs) have promising applications in long-term autofluorescence-free bioimaging due to the long and multiple activatable afterglow nature. Coating a mesoporous shell on the surface of PLNPs is a usual way to give PLNPs additional drug loading capability, but often leads to the reduction of afterglow luminescence. Herein, we report the fabrication of hyaluronic acid (HA) grafted near-infrared (NIR) PLNP with hollow nanocage structure (PLNC) without the need for an additional mesoporous coating for enhanced targeted autofluorescence-free afterglow imaging and nanocarrier mediated drug delivery to treat bacterial infection. The PLNC was prepared by calcinating solid Cr-doped $MgSn(OH)_6$ in a reducing atmosphere. The as-synthesized PLNC not only gave better persistence luminescence than solid Cr-doped zinc gallogermanate PLNPs for autofluorescence-free bioimaging, but also possessed mesoporous structure as a nanocarrier for drug delivery. As a proof of concept, antimicrobial drug rifampicin (RIF) loaded amino modified PLNC (PLNC-NH_2) was prepared for antimicrobial application. RIF loaded PLNC-NH_2 was further modified with hyaluronic acid (HA) to make RIF loaded PLNC-HA selectively target to the site of bacterial infection. The developed RIF loaded PLNC-HA not only exhibited efficient antimicrobial therapeutic effects, but also provided autofluorescence-free targeted afterglow imaging of the infection site for guided therapy. This work provides a new simple way for the synthesis of mesoporous PLNCs with additional drug delivery function for nanotheranostic application.

1. Introduction

Persistent luminescent nanoparticles (PLNPs) are special optical nanomaterials that can store the energy of excitation light during excitation and persistently emit phosphorescence after the stop of irradiation [1,2]. This unique optical property enables PLNPs to avoid autofluorescence interference and significantly improve sensitivity for bioimaging [3,4]. Introducing therapeutic functions into PLNPs to prepare composites with integrated diagnosis and treatment attracts increasing attention in biomedical science [5,6]. Surface coating of PLNPs with additional mesoporous layers (such as mesoporous SiO_2 and MOFs) provides drug loading capability for PLNPs, but requires complex shell layer coating manipulation [7–10]. The shell coating operation often leads to the decrease in the afterglow luminescence of the PLNPs [11–13]. In addition, mesoporous SiO_2 coated PLNPs (PLNPs@SiO_2) usually have irregular morphology [14–16] and large particle size (more than 100 nm), which may make the drug delivery ability of the materials uncontrollable. In situ growth of PLNPs inside the pores of mesoporous SiO_2 under calcination is an another approach to obtain composite carriers with drug loading capacity (SiO_2@PLNPs) [17]. However, the drug loading function of the prepared composite carriers was unavoidably inhibited due to the blockage of the pore channels of mesoporous SiO_2 by the generated tiny PLNPs. Therefore, it is crucial to prepare PLNPs with uniform morphology, small particle size, strong afterglow luminescence, and drug-carrying structure.

Cr-doped stannate PLNPs have good afterglow imaging capability due to long NIR emission wavelengths for deep penetration imaging [18,19]. Unlike the afterglow emission of Cr-doped zinc gallogermanate

* Corresponding author at: State Key Laboratory of Food Science and Resources, Jiangnan University, Wuxi 214122, China.
E-mail address: xpyan@jiangnan.edu.cn (X.-P. Yan).

https://doi.org/10.1016/j.cej.2023.147740
Received 8 September 2023; Received in revised form 6 November 2023; Accepted 27 November 2023
Available online 7 December 2023

PLNP (ZGGO) (700 nm) close to the edge of the first tissue transparency window (650–900 nm) [20], Cr-doped stannate PLNP have a wide 650–1000 nm emission for deep penetration imaging [21]. In addition, compared with ZGGO, stannate PLNP is more suitable for mass production because of lower costs. Current stannate PLNP is mainly synthesized by solid-phase methods, but the particle size of the synthesized material is too large for in vivo imaging [22–24]. Hydrothermal heating of a mixture of metal ions and ammonia to synthesize Cr and Eu co-doped Zn_2SnO_4 PLNP (*ca.* 7 nm) shows great promising for in vivo imaging [25]. Even so, these Cr-doped stannate PLNPs themselves do not provide additional drug delivery function.

Herein, we show a simple strategy to synthesize mesoporous Cr-doped tin-based persistent luminescence nanocage (PLNC) with both excellent NIR persistent luminescence and drug loading capability for targeted afterglow imaging and therapy of bacterial infection. The PLNC is prepared by calcinating solid Cr-doped $MgSn(OH)_6$ in an oxygen-free atmosphere without the need for additional coating of mesoporous shells. The as-synthesized PLNC not only gives better persistence luminescence than solid Cr-doped zinc gallium germanate PLNP (ZGGO) for autofluorescence-free bioimaging, but also possesses mesoporous structure as nanocarrier for drug delivery. As a proof of concept, antimicrobial drug rifampicin (RIF) loaded amino modified PLNC (PLNC-NH_2) is prepared for antimicrobial application. Further modification of RIF loaded PLNC-NH_2 with hyaluronic acid (HA) makes RIF loaded PLNC-HA selectively target to the site of bacterial infection. The developed RIF loaded PLNC-HA not only exhibits efficient antimicrobial therapeutic effects, but also provides autofluorescence-free targeted afterglow imaging guided therapy of bacterial infection.

2. Materials and methods

2.1. Materials and chemicals

$Mg(NO_3)_2{\cdot}6H_2O$ (99.99%), $SnCl_4{\cdot}5H_2O$ (99.99%), $Cr(NO_3)_3{\cdot}9H_2O$ (99.99%), 1-(3-dimethylaminopropyl)-3-ethylcarbodiimide hydrochloride (EDC•HCl), N-hydroxysulfosuccinimide (NHS), RIF, and HA were purchased from Sinopharm Chemical Reagent Co. (Shanghai, China). Ga_2O_3 (99.99%), $Yb(NO_3)_3{\cdot}5H_2O$ (99.9%), $Er(NO_3)_3{\cdot}5H_2O$ (99.9%), and dimethyl sulfoxide were purchased from Aladdin (Shanghai, China). Phosphate-buffer saline (PBS) (premixed powder), Luria Bertani (LB) broth powder (FMB Grade), hyaluronidase (HAase), and LB agar powder (FMB Grade) were purchased from Shanghai Sangon Biotech (Shanghai, China). Methicillin-resistant Staphylococcus aureus was obtained from the Collaborative Innovation Center of Radiological Medicine of Jiangsu Higher Education Institutions (Suzhou, China). Ultrapure water was acquired from Wahaha Group Co (Hangzhou, China).

2.2. Characterization

Transmission electron microscopy (TEM) images were taken on a JEM-2100 transmission electron microscope (JEOL, Japan). High-resolution TEM images, high angle annular dark field scanning (HAADF-STEM), and elemental mapping images were obtained on a JEM-F200 transmission electron microscope (JEOL, Japan). Luminescence measurements were performed on an F-7000 spectrofluorometer (Hitachi, Japan). UV–vis absorption spectra were obtained on a UV-3600plus spectrophotometer (Shimadzu, Japan). Fourier transform infrared (FT-IR) spectra were obtained on a Nicolet IS10 spectrometer (Thermo Scientific, USA) with a KBr pellet. Zeta potential and hydrodynamic size distribution were obtained on the Nano-ZSE Zetasizer (Malvern Panalytical, UK). A D2 PHASER diffractometer (Bruker, Germany) was used to record X-ray diffraction (XRD) patterns. Autosorb-iQ (Quantachrome, USA) was used for N_2 adsorption experiments at 77 K. Afterglow luminescence imaging experiments were carried out on an IVIS Lumina XRMS Series III Imaging System (Perkin Elmer, USA). An Olympus FV3000 confocal laser scanning microscope (Japan) was used to collect fluorescent bacterial stains.

2.3. Synthesis of PLNC and ZGGO

$Mg(NO_3)_2{\cdot}6H_2O$ (2 mmol), $SnCl_4{\cdot}5H_2O$ (1 mmol), and $Cr(NO_3)_3{\cdot}9H_2O$ (0.01 mmol) were dissolved in ultrapure water (10 mL). Then, aqueous ammonia (0.5 mL, 25%) was dropped into the above solution and kept stirring for 30 min. Subsequently, the precursor solution was transferred into a Teflon-lined autoclave and heated at 220 °C for 24 h. The product Cr-doped $MgSn(OH)_6$ was centrifugated, washed with ultrapure water three times, and dried at 60 °C. Then, the dried Cr-doped $MgSn(OH)_6$ was calcined at 600 °C for 1 h with a heating rate of 5 °C min^{-1} in oxygen-free atmosphere provided by activated carbon to obtain the PLNC.

Solid ZGGO was synthesized according to our previous work for comparison [26].

2.4. Preparation of RIF loaded PLNC-HA and PLNC-HA

RIF loaded PLNC-HA was prepared as follows: Amino-modified PLNC was prepared as described in Supplementary Information. The prepared amino-modified PLNC (50 mg) was added to the methanol solution of RIF (50 mL, 2 mg mL^{-1}) and stirred for 12 h to obtain RIF loaded PLNC-NH_2. HA (200 mg) was dissolved in ultrapure water (100 mL) and stirred overnight, followed by adding NHS (800 mg) and EDC•HCl (400 mg). The mixture was stirred for 1 h to activate the –COOH of HA. Subsequently, the prepared methanol solution of RIF loaded PLNC-NH_2 was added to the above HA solution and stirred for 12 h. The resulting product was washed with ultrapure water three times and then collected by centrifugation to obtain RIF loaded PLNC-HA.

PLNC-HA was prepared as described for RIF loaded PLNC-HA but without loading RIF to test the cytotoxicity.

2.5. Stability study

To test the stability of PLNC, the prepared PLNC was dispersed in PBS (10 mmol/L, pH 7.4), then the afterglow images and the hydrodynamic diameter of the solution of PLNC were collected on days 1, 2, 3, 5, 7, and 10, respectively. To further test the stability of RIF loaded PLNC-HA, the FT-IR spectra and the hydrodynamic diameter of the RIF loaded PLNC-HA were collected on days 1, 3, 5, 7, and 10, respectively.

2.6. RIF release experiments

RIF loaded PLNC-HA (20 mg as PLNC) was dispersed in simulated infected tissue environment (PBS (10 mL, 10 mmol/L, pH 5.5), 150 U mL^{-1} HAase) and simulated normal tissue environment (PBS (10 mL, 10 mmol/L, pH 7.4), no HAase), respectively. The mixture was incubated at 37 ℃ and centrifuged (10,000 r min^{-1}) at predetermined times (2, 4, 6, 12, 24, and 48 h), then 1 mL of the solution was taken out to measure the absorbance for the characteristic absorption peak of RIF at 470 nm for the determination of the amount of RIF released, meanwhile 1 mL of fresh corresponding buffer was added for subsequent measurement.

2.7. In vivo afterglow imaging testing of PLNC

Balb/c mice (female, five weeks) were purchased from Changzhou Cavens Laboratory Animal Co. Ltd (Changzhou, China). All animal studies were approved by the Animal Ethics Committee of Jiangnan University (JN.No. 20230515b0250622[1 7 3]), and conducted according to the Guidelines for the Use and Care of Laboratory Animals of Jiangnan University. Balb/c mice were intravenously injected with 200 μL of PBS (10 mmol/L, pH 7.4) containing PLNC (4 mg mL^{-1}). The mice were then illuminated with 650 nm LED light and the afterglow images of the mice were acquired five times to determine the stability of PLNC for in vivo imaging. To compare in vivo optical performance of ZGGO

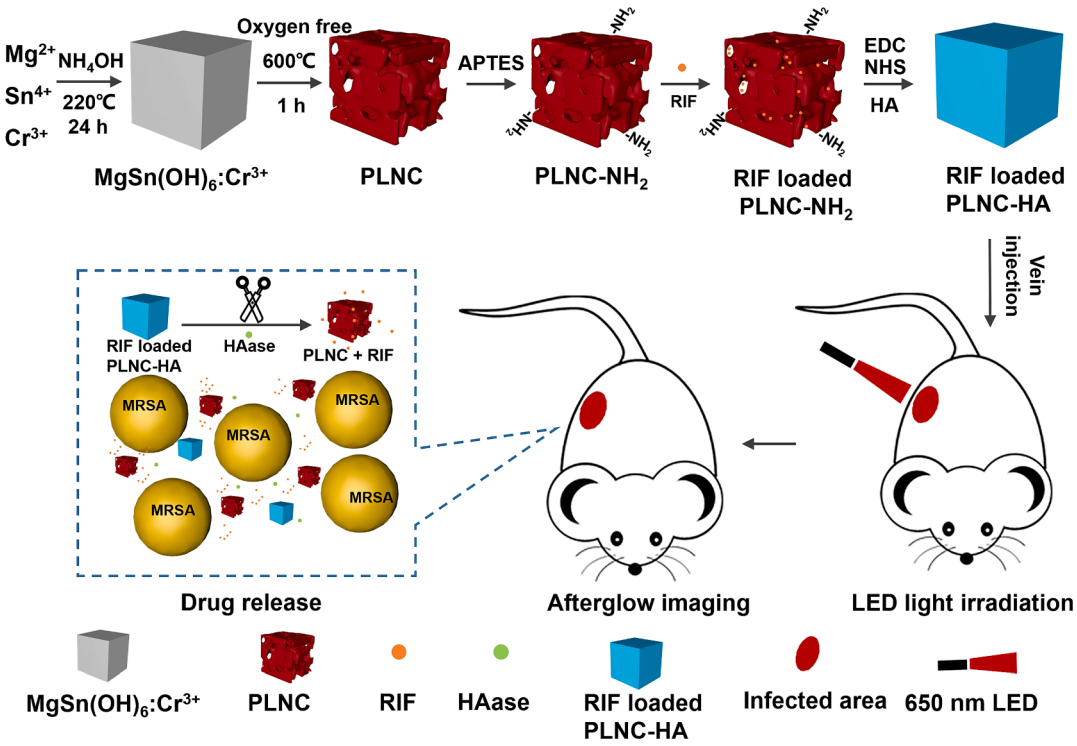

Scheme 1. Illustration for the synthesis of PLNC for the afterglow imaging and the treatment of bacterial infections.

and PLNC, Balb/c mice were subcutaneously injected with ZGGO (1 mg mL^{-1}, 100 μL) and PLNC (1 mg mL^{-1}, 100 μL), and then the afterglow images were acquired. All the mice were irradiated with 650 nm LED light for 2 min before acquiring afterglow images.

2.8. Bacterial culture and in vitro antibacterial test

Methicillin-resistant *Staphylococcus aureus* (MRSA) and LB broth were at 37 °C for 12 h. The bacterial broth was centrifuged and resuspended in LB broth (pH 5.5) to obtain the concentration of 2×10^8 CFU mL^{-1}. 500 μL LB broth (pH 5.5) containing RIF loaded PLNC-HA and 500 μL LB broth (pH 5.5) containing 2×10^8 CFU MRSA cells were mixed for 12 h incubation. 100 μL of each diluted sample was plated on plates for 12 h incubation at 37 °C. The colonies produced on the plates were counted to evaluate bacterial concentration.

2.9. Afterglow imaging experiments of infected mice

MRSA in PBS (10 mmol/L, pH 7.4) (150 μL, ~10^8 CFU mL^{-1}) was injected subcutaneously into the back of each mouse to establish a subcutaneous abscess mouse model. To test the targeting ability of RIF loaded PLNC-HA, the infected mice were intravenously injected with RIF loaded PLNC (4 mg mL^{-1} as PLNC, 200 μL) and RIF loaded PLNC-HA (4 mg mL^{-1} as PLNC, 200 μL), respectively. Then, the afterglow images of mice were acquired at different time points (12 h, day 1, day 2, and day 3) after injection.

To show the ability of RIF loaded PLNC-HA for targeted imaging over a longer period, the infected mice were intravenously injected with 200 μL RIF loaded PLNC-HA (4 mg mL^{-1} as PLNC). Then, the afterglow images of mice were acquired at different time points (5 min, 12 h, days 1, 2, 3, 5, 7, 9, and, 11). All the mice were irradiated with 650 nm LED light for 2 min before acquiring afterglow images.

2.10. In vivo antibacterial therapy

The infected mice were randomly divided into three groups ($n = 5$ per group): PBS (control, 200 μL), RIF (0.96 mg mL^{-1}, 200 μL), and RIF loaded PLNC-HA (4 mg mL^{-1} as PLNC, 200 μL), and intravenously injected into the mice. Mouse weights were weighed and recorded daily during treatment. Photographs of the infected site were recorded on days 0, 1, 3, 5, 7, 9, and 11, and the infected area was evaluated using Image J software. On day 11, all mice were sacrificed, and then the infected skin, heart, liver, spleen, lung, and kidney of the mice were collected and stored in 4% paraformaldehyde. Tissue sections and the histology and immunohistochemistry assays of the sections were technically supported by Erwan Biological Co. (Suzhou, China).

2.11. Biodistribution of RIF loaded PLNC-HA

After the tail vein injection of the RIF loaded PLNC-HA (4 mg mL^{-1}, 200 μL) for 24 h, the mice were sacrificed to acquire the main organs (liver, heart, spleen, lung, and kidney). Then, the organs were irradiated with 650 nm light for 2 min to collect the luminescence signal.

3. Results and discussion

3.1. Preparation and characterization of RIF loaded PLNC-HA

Scheme 1 shows the procedure and principle for the synthesis and application of RIF loaded PLNC-HA for autofluorescence-free targeted afterglow imaging guided therapy of bacterial infection. Highly dispersed precursor material (Cr-doped $MgSn(OH)_6$) was first prepared by a hydrothermal method. Calcinating Cr-doped $MgSn(OH)_6$ gave mesoporous PLNC under the calcination in a reducing atmosphere to avoid the oxidation of Cr(III) to Cr(VI) (Fig. S1) [27]. The PLNC was further aminated to give PLNC-NH_2 for subsequent HA grafting. RIF was then loaded onto mesoporous PLNC-NH_2 to obtain RIF loaded PLNC-NH_2. Further HA grafting of RIF loaded PLNC-NH_2 via the reaction between the –NH_2 in PLNC-NH_2 and the –COOH in HA to obtain RIF-loaded PLNC-HA. The grafted HA enables specific binding to the clusters of differentiation 44 (CD44) receptors overexpressed in macrophages at the site of infection for targeted imaging [28]. In addition, the

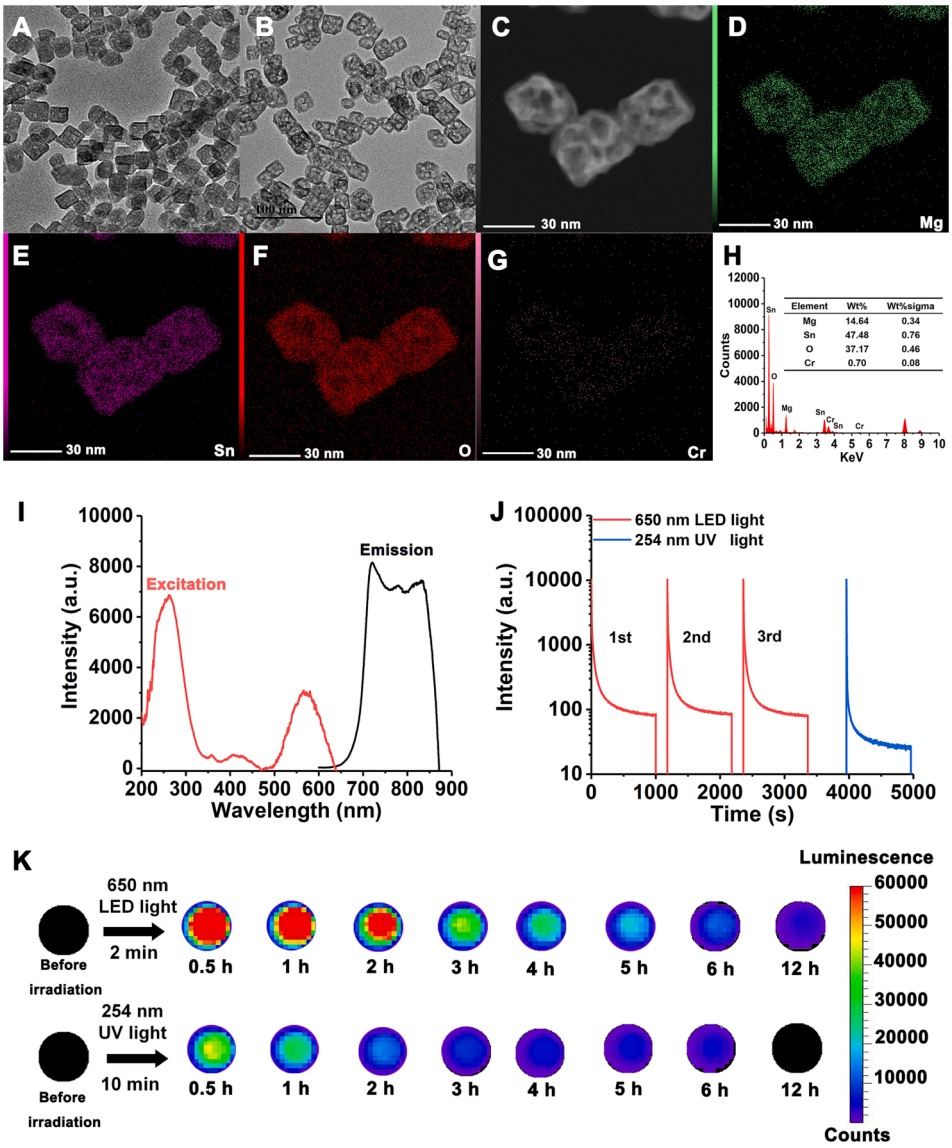

Fig. 1. (A) TEM images of Cr-doped $MgSn(OH)_6$. (B) TEM images of the PLNC. (C-G) Element mapping images and (H) EDS analysis for the PLNC. (I) Excitation and emission spectra of the PLNC powder. (J) NIR afterglow decay curve of PLNC powder after 2-min of excitation by a 650 nm LED light three times and 10 min of excitation at 254 nm UV light, respectively. (K) Afterglow images of the PLNC powder after 2-min excitation by a 650 nm LED light and 10-min excitation by a 254 nm UV light, respectively.

overexpressed hyaluronidase (HAase) at the site of infection can degrade the surface-covered HA [29], resulting in the release of RIF for the therapy of bacterial infection.

The synthesis conditions (calcination temperature, the content of doped Cr, and calcination time) were optimized to prepare PLNC with high afterglow luminescence intensity and good hollow structure (Fig. S2–S9, Table S1 and S2). The optimal calcination temperature, calcination time, and Cr-doped content were 600 °C, 1 h, and 0.01 mmol, respectively.

The as-prepared Cr-doped $MgSn(OH)_6$ and PLNC were characterized by TEM, XRD, dynamic light scattering, and N_2 adsorption experiments. Both Cr-doped $MgSn(OH)_6$ and PLNC exhibited cubic shape, similar solid size (26.0 ± 3.6 nm and 26.9 ± 4.6 nm, respectively), hydrodynamic diameter (ca. 100 nm) (Fig. S10), and BET surface area (90.5 and 92.4 $m^2\ g^{-1}$, respectively) (Table S1), but different pore volumes (0.335 and 0.539 $cm^3\ g^{-1}$, respectively) and pore size (ca. 3.7 and 4.2 nm, respectively) (Fig. S11). The characteristic diffraction peaks at 19.8° (111), 22.9° (200), and 32.6° (220) of as-prepared Cr-doped $MgSn(OH)_6$ indicate pure spinel phase $MgSn(OH)_6$ (PDF-number 09–0027, Fig. S12). The characteristic diffraction peaks at 17.8° (111), 29.2° (220), and 34.4° (311) of PLNC were consistent with the standard data of Mg_2SnO_4 (PDF-number 24–0723), while the peaks at 26.6° (110), 33.8° (101), and 37.9° (200) were consistent with the standard data SnO_2 (PDF-number 41–1445). Those results indicate that the as-prepared PLNC contained the phase of Mg_2SnO_4 and SnO_2 (Fig. S12). Those results indicate that calcination made the small cavities inside the Cr-doped $MgSn(OH)_6$ change into obvious hollow structure of PLNC (Fig. 1A and B). In addition, calcination changed Cr-doped $MgSn(OH)_6$ from no luminescence to obvious afterglow luminescence of PLNC under both 254 nm and 650 nm light irradiation (Fig. S13). Compared to PLNPs@SiO_2 [30], the prepared PLNC showed more homogeneous morphology as well as smaller particle size. In addition, the BET surface area of the prepared PLNC (92.4 $m^2\ g^{-1}$) is larger than that of the SiO_2@PLNPs (ca. 20 $m^2\ g^{-1}$) [31,32].

The as-synthesized PLNC gave clear lattice fingerprints of (111) plane of Mg_2SnO_4 and lattice fingerprints of (101) plane of SnO_2 (Fig. S14). The HAADF STEM and elemental mapping images, and energy dispersive spectroscopy analysis verified the presence of Mg (14.64

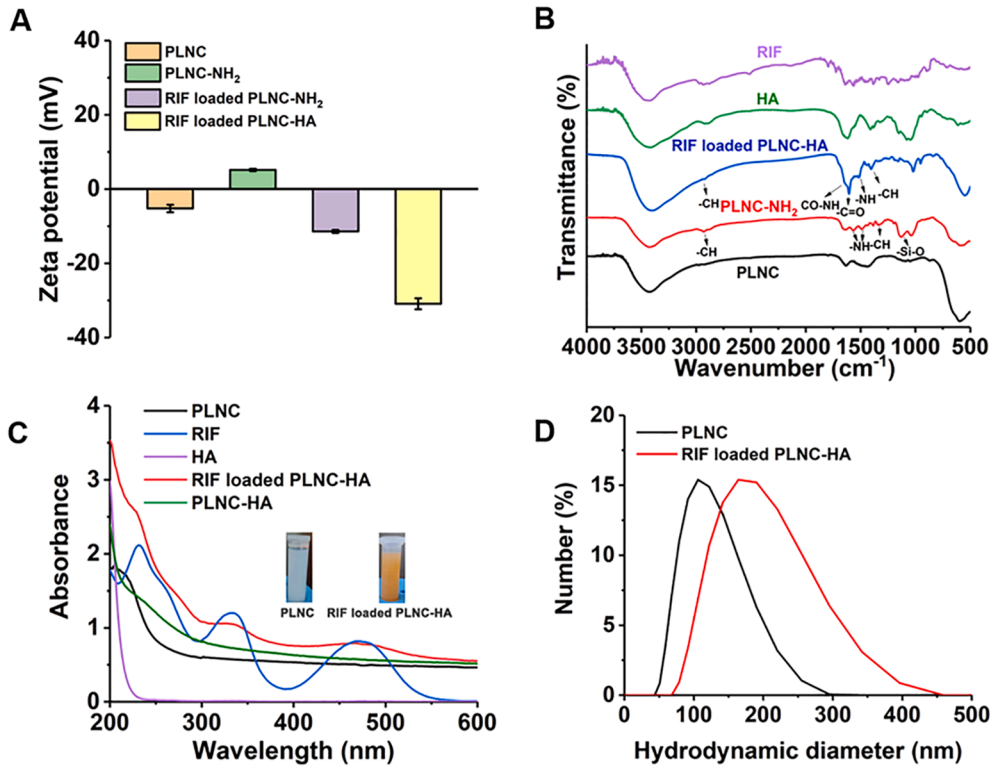

Fig. 2. (A) Zeta potential of PLNC, PLNC-NH_2, RIF loaded PLNC-NH_2, and RIF loaded PLNC-HA. (B) FT-IR spectra of RIF, HA, PLNC, PLNC-NH_2, and RIF loaded PLNC-HA. (C) UV–vis absorption spectra of RIF, HA, PLNC, PLNC-HA, and RIF loaded PLNC-HA (insert: photograph of PLNC aqueous solution and RIF-loaded PLNC-HA aqueous solution). (D) Hydrodynamic diameter of PLNC and RIF loaded PLNC-HA.

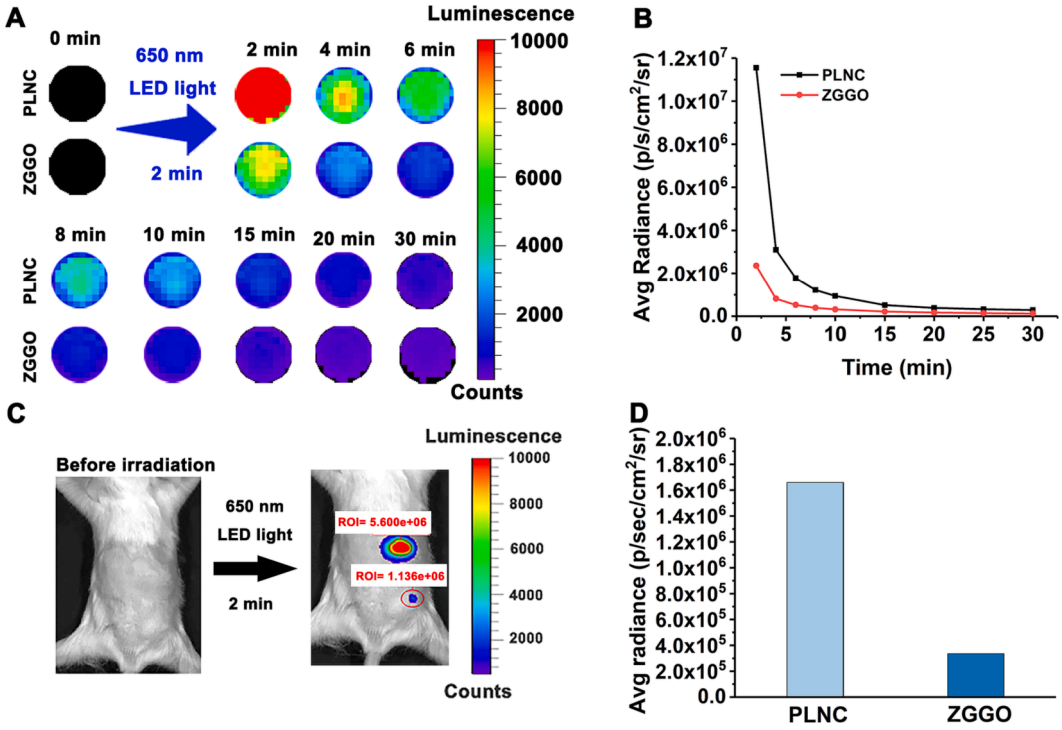

Fig. 3. (A) Afterglow images of the PLNC aqueous solution (1 mg mL^{-1}) and the ZGGO aqueous solution (1 mg mL^{-1}). PLNC and ZGGO aqueous solution (1 mg mL^{-1}) were excited by a 650 nm LED light for 2 min, then the afterglow luminescence images were recorded at different time points (2 min, 4 min, 6 min, 8 min, 10 min, 15 min, 20 min, and 30 min). (B) Change of afterglow intensity with time for PLNC and ZGGO (LED 2 min). (C) In vivo afterglow images after subcutaneous injection of PLNC (1 mg mL^{-1}) (upper) and ZGGO (1 mg mL^{-1}) (lower) into the back of the mouse. The nanoparticles were dispersed in 0.1 mL PBS (pH 7.4, 10 mmol/L). The afterglow images were acquired after the mouse was irradiated by 650 nm light for 2 min. (D) Average afterglow luminescence intensity of PLNC and ZGGO in the back of the mouse from (C).

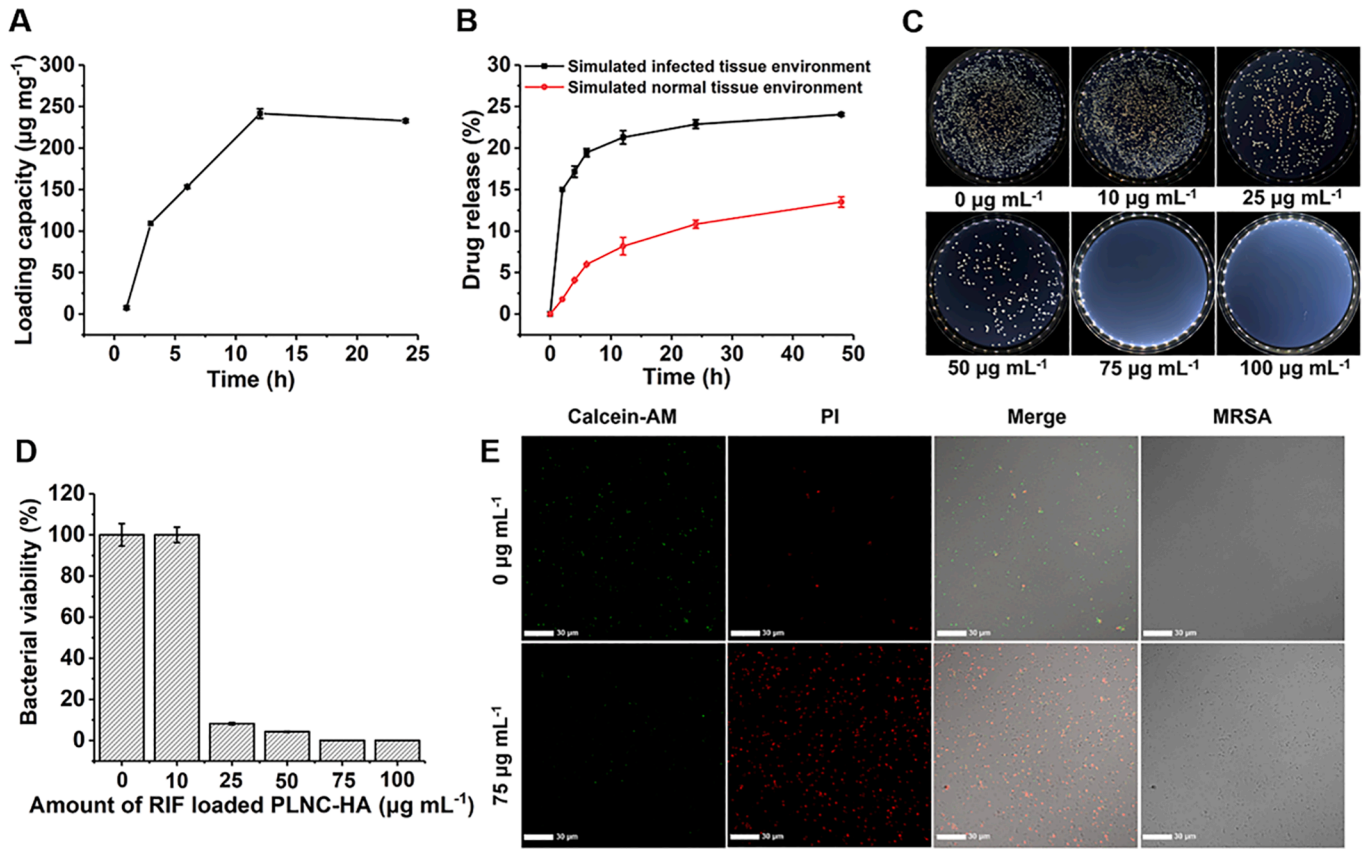

Fig. 4. (A) Effect of loading time on drug loading capacity. (B) Sustained-release property of RIF loaded PLNCs-HA in simulated infected tissue environment buffer and simulated normal tissue environment buffer, respectively. (C) Photographs of bacterial colonies after incubation with different concentrations of RIF loaded PLNC-HA. (D) Bacterial viability of MRSA incubated with different concentrations of RIF loaded PLNC-HA. (E) Fluorescent images of live/dead bacterial staining of MRSA treated with 0 (control group) and 75 μg mL^{-1} RIF loaded PLNC-HA.

%), Sn (47.48 %), O (37.17 %), and Cr (0.7 %) elements uniform distributed in the PLNC (Fig. 1D–H). In addition, XPS spectra showed the peaks of Mg 1 s at 1301 eV [33], O1s at 527.5 eV, Sn 3d3/2 at 483.7 eV, and Sn 3d5/2 at 492.1 eV [34] (Fig. S15). These results further indicate that PLNC are composed of SnO_2 and Mg_2SnO_4.

The excitation spectra of the PLNC showed three peaks at 357 nm, 407 nm, and 565 nm from the doped Cr^{3+} (Fig. 2A) [35]. Under 254 nm UV light excitation, the PLNC exhibited a broad emission from 600 nm to 870 nm due to the contribution from both the broadband NIR emission of the spin-allowed transition from the Cr^{3+} $^4T_2(4F) \rightarrow {}^4A_2$ (ca. 830 nm) as well as the narrow peak (ca. 720 nm) from the spin-forbidden transition of Cr^{3+} $^2E \rightarrow {}^4A_2$ [36]. The wide emission of the PLNC gives PLNC more deep penetration imaging ability compared to ZGGO [18,19]. The PLNC emitted afterglow luminescence after the irradiation of both 254 nm and 650 nm light and the afterglow luminescence was reactivatable by a 650 nm LED light (Fig. 2B and C). The excellent 650 nm reactivation capability allows the PLNC to be repeatedly activated by NIR light for in vivo afterglow luminescence imaging application.

Amino-modification of the PLNC increased the zeta potential from −5.2 mV to + 5.2 mV (Fig. 2A), and gave additional FT-IR peaks such as stretching vibration of -Si-O at 1129 cm^{-1}, stretching bands of N-H at 1490 and 1640 cm^{-1}, and –CH stretching vibrations at 1334 and 2930 cm^{-1} (Fig. 2B) [37]. Compared to PLNC-NH_2, RIF loaded PLNC-NH_2 and RIF loaded PLNC-HA showed negative zeta potential (-11.4 and −30.9 mV, respectively) again, and typical FT-IR characteristic peaks such as two bands of CO-NH and –COO at 1632 cm^{-1} [38], RIF characteristic absorption band in UV–vis absorption spectra (Fig. 2C), indicating the successful load of RIF and grafting of HA. While the hydrodynamic diameter of RIF loaded PLNC-HA significantly increased after the grafting of HA compared to PLNC (Fig. 2D). All these results further confirmed the success of surface modification.

3.2. Comparison of the afterglow imaging abilities of PLNC and ZGGO

Compared with our previously synthesized ZGGO [26], the synthesized PLNC shows better afterglow luminescence under 650 nm LED light activation. The synthesized PLNC exhibited about 5.0 times higher afterglow luminescence intensity than ZGGO after 650 nm light excitation for 2 min (Fig. 3A and B). The afterglow luminescence intensity of PLNC was also consistently higher than that of ZGGO for the next 30 min. In vivo imaging also revealed the stronger afterglow luminescence signal of the PLNC than ZGGO (*ca.* 5.0 times) after 650 nm light irradiation for 2 min (Fig. 3C and D).

To further demonstrate the advantages of PLNC in long-term afterglow imaging, long-term afterglow imaging experiments were performed. Under the irradiation of 254 nm UV light, PLNC exhibited lower afterglow luminescence intensity than ZGGO, but showed stronger reactivated afterglow luminescence intensity by a 650 nm LED light at 24 h and 48 h (Fig. S16 and S17). As shell coating usually leads to the decrease in the afterglow luminescence of the PLNPs [11–13], the prepared PLNC gave stronger afterglow signals than the reported drug-loading composites constructed based on ZGGO and SiO_2 for imaging.

3.3. Stability and biocompatibility of PLNC and RIF loaded PLNC-HA

To demonstrate the suitability of PLNC for in vivo bioimaging, the stability and biocompatibility of the PLNC and RIF loaded PLNC-HA were investigated. PLNC was incubated in PBS (pH 7.4, 10 mmol/L) for 10 d, and then the changes in hydrodynamic diameter and the afterglow intensity of the PLNC were investigated to test the stability

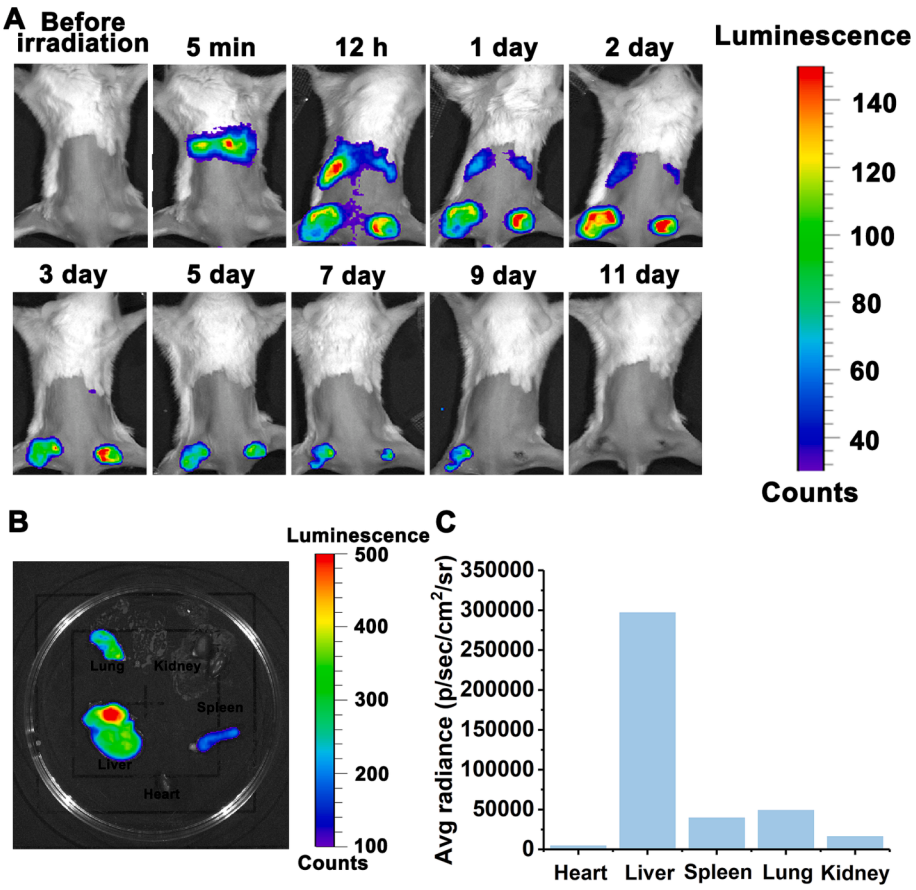

Fig. 5. (A) Afterglow images of the infected mice at different times (before irradiation, 5 min, 12 h, and days 1, 2, 3, 5, 7, 9, and 11) with the injection of RIF loaded PLNC-HA. (B) Afterglow images of major organs of the mice after being injected with RIF loaded PLNC-HA for 24 h. (C) Afterglow intensity of major organs of the mice after injection of RIF loaded PLNC-HA for 24 h.

(Fig. S18A and B). No significant changes in the phosphorescence spectra, hydrodynamic diameter of the PLNC were observed after 10 d incubation, showing the good stability of the PLNC. The hydrodynamic diameter and FT-IR spectra of RIF loaded PLNC-HA also did not show obvious changes after 10 d incubation, indicating that the synthesized nanocarrier had good stability for in vivo bioimaging applications (Fig. S18C and D).

The toxicity of the PLNC and PLNC-HA nanocarrier was evaluated by the MTT method. The survival rate of the 3T3 cells remained over 90% when the concentration of the PLNC and PLNC-HA reached 1 mg mL^{-1}, indicating that both PLNC and PLNC-HA did not have significant cytotoxicity (Fig. S19A and B). Next, a hemolysis test was used to further assess the biocompatibility of PLNC and PLNC-HA. The results indicate that the hemolysis of PLNC and PLNC-HA was below 10% even when the concentration of PLNC and PLNC-HA reached 1 mg mL^{-1}, indicating the low risk of hemolysis (Fig. S19C and D). These results suggest the good biocompatibility of the PLNC and the PLNC-HA for biomedical imaging in vivo.

3.4. Drug loading and release study

The RIF loading and release capacities of the PLNC were studied by UV–vis spectrometry. The loading capacity increased in the first 12 h, then became unchanged. The maximum loading capacity of PLNC for RIF was measured to be 241 μg mg^{-1} (Fig. 4A). Cumulative drug release of RIF loaded PLNC-HA was comparatively investigated in the simulated infected tissue environment (PBS (10 mL, 10 mmol/L, pH 5.5), 150 U mL^{-1} HAase) and simulated normal tissue environment (PBS (10 mL, 10 mmol/L, pH 7.4), no HAase) (Fig. 4B). After incubation for 48 h, 24% of the loaded RIF was released in the simulated infected tissue environment, whereas only 13% the loaded RIF was released in the simulated normal tissue environment.

3.5. In vitro antibacterial

MRSA, a pathogen of public health significance, was selected to explore the antimicrobial ability of RIF loaded PLNC-HA by the plate count method and the living/dead bacteria staining method. The effect of PLNC and PLNC-HA on the viability of MRSA was first tested. The results show that both PLNC and PLNC-HA exhibited no obvious antibacterial effect (Fig. S20). The effect of the concentration of RIF loaded PLNC-HA on the antibacterial activity was further examined in the range of 0–100 μg mL^{-1}. When MRSA bacteria were incubated with PLNC-RIF-HA, the HA attached to the surface of PLNC was broken down due to the HAase secreted by MRSA to release the RIF from the pore for killing the bacteria. Thus, the number of bacterial colonies significantly decreased as the concentration of RIF loaded PLNC-HA increased (Fig. 4C-D). The bacterial kill rate reached 91.9 % in the presence of 25 μg mL^{-1}, and the growth of the bacteria was entirely prevented in the presence of 75 μg mL^{-1} RIF loaded PLNC-HA. The antibacterial ability of RIF loaded PLNC-HA was further demonstrated by the living/dead bacteria staining method. Calcein-AM is a kind of fluorescence probe that can pass through cell membrane and remove the AM group by esterases in living cells, resulting in calcein that emits a strong green fluorescence, thus living cells can be detected under a fluorescence microscope as green fluorescence. Propidium iodide (PI) can pass through damaged cell membrane and enter dead cells and embed itself in the cell's DNA double helix, emitting red fluorescence, thus dead cells can be detected

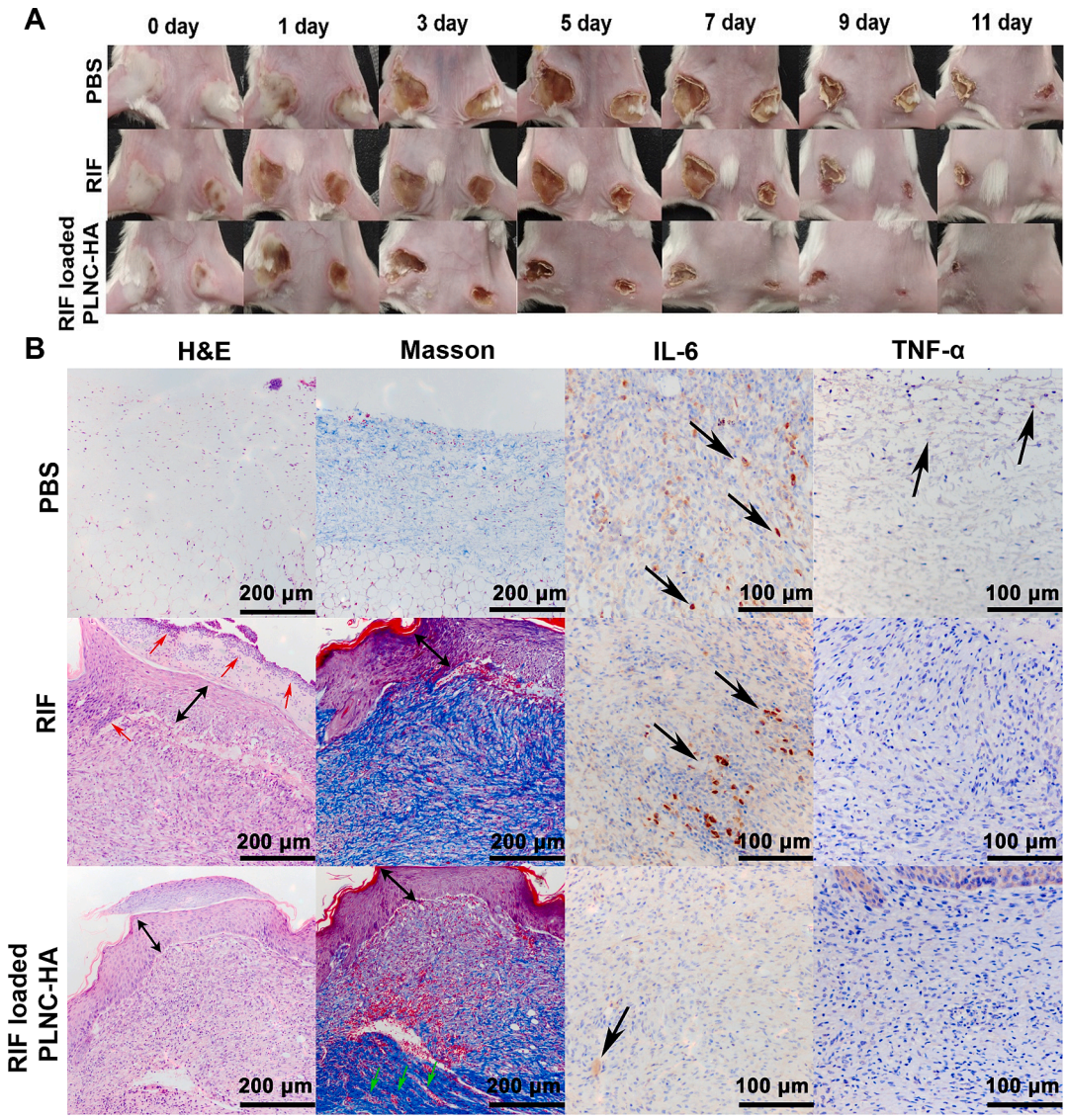

Fig. 6. (A) Photographs of infected sites in mice after different treatments on days 0, 1, 3, 5, 7, 9, and 11. (B) H&E, Masson, IL-6, and TNF-α staining of the skin tissue slices. The positive areas were marked by the black arrow. The epidermal structures are marked with the black double arrows. Capillary structures were marked by the green arrow. The inflammatory cells were marked by red arrow.

as red fluorescence. As shown in Fig. 4E, the bacteria in the control group (without RIF loaded PLNC-HA) showed significant green fluorescence but very little red fluorescence, indicating live bacteria. However, after treating with RIF loaded PLNC-HA for 12 h, the bacteria showed significant red fluorescence, indicating that the bacteria were killed. The results of live/dead staining showed that RIF loaded PLNC-HA could kill MRSA. Thus, the bactericidal properties of RIF loaded PLNC-HA derived from the release of antibiotic RIF.

3.6. *In vivo afterglow imaging and distribution of RIF loaded PLNC-HA*

The long-time targeted in vivo afterglow imaging ability of the RIF loaded PLNC-HA was further investigated. To this end, the RIF loaded PLNC and the RIF loaded PLNC-HA were injected into the infected mice via the tail vein, and afterglow luminescence signals were collected over several days for comparison. The mice injected with RIF loaded PLNC-HA showed a gradually enhanced afterglow luminescence from 12 h to 2 d in the abscess area, suggesting the accumulation of RIF loaded PLNC-HA in the infected region (Fig. 5A). In contrast, the mice injected with RIF loaded PLNC showed a much weaker afterglow luminescence signal in the abscess area, indicating that PLNC-HA has a good ability to specifically target to the site of infection (Fig. S21). In vivo afterglow images also showed that PLNC-HA can track wounds for 9 days. As the infected area gradually healed, the afterglow signal at the infected site gradually decreased and disappeared after the scabs fell off (Fig. 5A). The afterglow signal of RIF loaded PLNC-HA in the liver gradually decreased, while the afterglow signal in the feces of mice could be observed, indicating that RIF loaded PLNC-HA can be metabolized by the liver and excreted (Fig. S22). The afterglow signal observed from the fallen scab of mice shows that RIF loaded PLNC-HA at the wound can be excreted through this pathway. These results show that RIF loaded PLNC-HA not only enabled effective targeting to the infected site, but also provided imaging information for treatment. It could also be effectively excreted through feces and scabs. Compared to our previous system based on ZGGO and SiO_2 for the diagnosis and treatment of bacterial infections [39,40], the prepared PLNC-RIF-HA is more likely to accumulate at the site of bacterial infection, achieving stronger targeted afterglow imaging capability for bacterial infection. Next, the main organs (liver, heart, spleen, kidneys, and lung) of the mice were collected after intravenous injection of RIF loaded PLNC-HA for 24 h to study the biodistribution of RIF loaded PLNC-HA. The ex vivo afterglow image shows that the afterglow luminescence signal mainly occurred in the

liver, indicating that RIF loaded PLNC-HA could be captured by the liver (Fig. 5B and C). A weaker afterglow luminescence signal was found in the spleen, lung, and kidney compared to the liver region, which agrees well with the published results [41].

3.7. In vivo antibacterial therapy

To study the in vivo antibacterial therapy efficacy of RIF loaded PLNC-HA, infected mice were treated with PBS, RIF, and RIF loaded PLNC-HA, respectively. Then, the infected areas were photographed, and the area changes in the infected areas were calculated. Of the three groups studied, the mice in the PBS group exhibited the slowest skin recovery from the infected area (the area of the abscess was about 31% of the original abscess area on day 11). The mice in the RIF-treated group showed a faster recovery of their skin (the area of the abscess was about 14% of the original abscess area on day 11). In contrast, the ulcers of MRSA-infected mice in the RIF-loaded PLNC-HA treatment group almost disappeared as the area of the abscess decreased to 2%. The above results showed that RIF-loaded PLNC-HA had good antimicrobial therapeutic ability (Fig. 6A and Fig. S23). After treatment, the skin in the infected area of mice was collected and evaluated by H&E, Masson, and immune staining (TNF-α, IL-6) ((Fig. 6B and Fig. S24). The results of H&E staining showed that the infection was not effectively treated after PBS injection, while the skin was repaired in the RIF loaded PLNC-HA and RIF groups. In addition, a large number of inflammatory cells appeared in the RIF group and the epidermis in the RIF loaded PLNC-HA group exhibited a cleaner structure and more noticeable cellular stratification, suggesting RIF loaded PLNC-HA had a more effective therapeutic effect than RIF. The results of Masson staining showed that the fibroblasts at the wound in the PBS group only secreted a small amount of collagen, while more ordered fibers were observed in the RIF group and RIF loaded PLNC-HA group and the collagen fibers were denser and richer after RIF loaded PLNC-HA treatment. In addition, in contrast to the RIF group, the RIF loaded PLNC-HA group's epidermal structure was more pronounced, with visible cell stratification and the development of capillaries, indicating active healing. The staining results of IL-6 showed a large range of positive signals in the PBS group, a strong local positive signal in the RIF group, but only a weak positive signal of IL-6 in the RIF loaded PLNC-HA group. The results of TNF-α staining showed a weak positive signal at the infection sites in the PBS group, while no significant signal in the RIF and RIF loaded PLNC-HA groups. These results also indicate that RIF loaded PLNC-HA had a good therapeutic effect.

The H&E analysis of major organs showed that RIF loaded PLNC-HA has no obvious damage to organs (Fig. S25). No significant weight loss was seen using RIF loaded PLNC-HA for treatment (Fig. S26). These results indicate that the RIF loaded PLNC-HA have acceptable biosafety for drug delivery and antibacterial therapy.

4. Conclusion

In conclusion, we have shown a simple strategy for the preparation of a novel mesoporous PLNC with excellent NIR afterglow luminescence and drug-carrying capability. The prepared PLNC can carry antibacterial drugs without the need for an additional coating of mesoporous shells. Based on the mesoporous PLNC, a RIF loaded PLNC-HA nanoplatform has been further developed for target afterglow imaging guided infection therapy. The excellent NIR-emitting afterglow and targeting ability of the RIF loaded PLNC-HA nanoplatform allow autofluorescence-free target bioimaging. The HA modified on the PLNC surface can be degraded by HAase at the site of infection, allowing the nanoplatform to release drug at the site of infection. This work provides a promising way for the synthesis of functionalized long afterglow nanoplatform without the need for an additional mesoporous coating for enhanced targeted autofluorescence-free afterglow imaging and nanocarrier mediated drug delivery to treat bacterial infection. Further efforts should focus on the studies on the exceptional pore structure of PLNC with new therapeutic approaches in clinical applications.

Declaration of competing interest

The authors declare that they have no known competing financial interests or personal relationships that could have appeared to influence the work reported in this paper.

Data availability

Data will be made available on request.

Acknowledgments

Financial support from the National Natural Science Foundation of China (No. 21934002, 22304063), and the Program of "Collaborative Innovation Center of Food Safety and Quality Control in Jiangsu Province" is highly appreciated.

Appendix A. Supplementary data

Supplementary data to this article can be found online at https://doi.org/10.1016/j.cej.2023.147740.

References

[1] K. Huang, N. Le, J.S. Wang, L. Huang, L. Zeng, W.C. Xu, Z. Li, Y. Li, G. Han, Designing next generation of persistent luminescence: recent advances in uniform persistent luminescence nanoparticles, Adv. Mater. 34 (2022) 2107962, https://doi.org/10.1002/adma.202107962.
[2] S.-K. Sun, H.-F. Wang, X.-P. Yan, Engineering persistent luminescence nanoparticles for biological applications: from biosensing/bioimaging to theranostics, Acc. Chem. Res. 51 (2018) 1131–1143, https://doi.org/10.1021/acs.accounts.7b00619.
[3] M. Sun, C. Yin, Z. Yan, Z.-J. Wei, Z. Zhang, W. Wang, Z. Yuan, Energy recruitment via lanthanide-chelate to boost the persistent luminescence of nanophosphor for contrast-enhanced tumor navigation, Chem. Eng. J. 468 (2023), 143814, https://doi.org/10.1016/j.cej.2023.143814.
[4] J. Wang, Q. Ma, Y. Wang, H. Shen, Q. Yuan, Recent progress in biomedical applications of persistent luminescence nanoparticles, Nanoscale 9 (2017) 6204–6218, https://doi.org/10.1039/C7NR01488K.
[5] D.L. Fritzen, L. Giordano, L.C.V. Rodrigues, J.H.S.K. Monteiro, Opportunities for persistent luminescent nanoparticles in luminescence imaging of biological systems and photodynamic therapy, Nanomaterials 10 (2020) 2015, https://doi.org/10.3390/nano10102015.
[6] J. Liu, T. Lécuyer, J. Seguin, N. Mignet, D. Scherman, B. Viana, C. Richard, Imaging and therapeutic applications of persistent luminescence nanomaterials, Adv. Drug Deliver. Rev. 138 (2019) 193–210, https://doi.org/10.1016/j.addr.2018.10.015.
[7] Z.-H. Wang, J.-M. Liu, C.-Y. Li, D. Wang, H. Lv, S.-W. Lv, N. Zhao, H. Ma, S. Wang, Bacterial biofilm bioinspired persistent luminescence nanoparticles with gut-oriented drug delivery for colorectal cancer imaging and chemotherapy, ACS Appl. Mater. Interfaces 11 (2019) 36409–36419, https://doi.org/10.1021/acsami.9b12853.
[8] Z.-H. Wang, J.-M. Liu, N. Zhao, C.-Y. Li, S.-W. Lv, Y. Hu, H. Lv, D. Wang, S. Wang, Cancer cell macrophage membrane camouflaged persistent luminescent nanoparticles for imaging-guided photothermal therapy of colorectal cancer, ACS Appl. Nano Mater. 3 (2020) 7105–7118, https://doi.org/10.1021/acsanm.0c01433.
[9] Y. Lv, D. Ding, Y. Zhuang, Y. Feng, J. Shi, H. Zhang, T.-L. Zhou, H. Chen, R.-J. Xie, Chromium-doped zinc gallogermanate@zeolitic imidazolate framework-8: A multifunctional nanoplatform for rechargeable in vivo persistent luminescence imaging and pH-responsive drug release, ACS Appl. Nano Mater. 11 (2019) 1907–1916, https://doi.org/10.1021/acsami.8b19172.
[10] H. Zhao, G. Shu, J. Zhu, Y. Fu, Z. Gu, D. Yang, Persistent luminescent metal-organic frameworks with long-lasting near infrared emission for tumor site activated imaging and drug delivery, Biomaterials 217 (2019), 119332, https://doi.org/10.1016/j.biomaterials.2019.119332.
[11] L.-J. Chen, X. Zhao, Y.-Y. Liu, X.-P. Yan, Macrophage membrane coated persistent luminescence nanoparticle@MOF-derived mesoporous carbon core–shell nanocomposites for autofluorescence-free imaging-guided chemotherapy, J. Mater. Chem. B 8 (35) (2020) 8071–8083, https://doi.org/10.1039/D0TB01272F.
[12] T. Yao, G. Dong, S. Qian, Y. Cui, X. Chen, T. Tan, L. Li, Persistent luminescence nanoparticles/hierarchical porous ZIF-8 nanohybrids for autoluminescence-free detection of dopamine, Sens. Actuators, B 357 (2022), 131470, https://doi.org/10.1016/j.snb.2022.131470.
[13] S. Wu, Y. Li, R. Zhang, K. Fan, W. Ding, L. Xu, L. Zhang, Persistent luminescence-polypyrrole nanocomposite for dual-modal imaging and photothermal therapy of

mammary cancer, Talanta 221 (2021), 121435, https://doi.org/10.1016/j.talanta.2020.121435.
[14] D. Ding, S. Li, H. Xu, L. Zhu, S. Meng, J. Liu, Q. Lin, S.W. Leung, W. Sun, Y. Li, H. Chen, X-ray-activated simultaneous near-infrared and short-wave infrared persistent luminescence imaging for long-term tracking of drug delivery, ACS Appl. Mater. Interfaces 13 (14) (2021) 16166–16172, https://doi.org/10.1021/acsami.1c02372.
[15] P. Lin, J. Shi, L. Ming, Y. Sheng, L. Song, M. Hong, Y. Zhang, An intelligent persistent luminescence nanoplatform with high-efficiency O_2 utilization for continuous hypoxic tumors treatment, Chem. Eng. J. 442 (2022), 135638, https://doi.org/10.1016/j.cej.2022.135638.
[16] J. Yang, Y. Zhao, Y. Meng, H. Zhu, D. Yan, C. Liu, C. Xu, H. Zhang, L. Xu, Y. Li, Y. Liu, Irradiation-free photodynamic therapy in vivo induced by enhanced deep red afterglow within NIR-I bio-window, Chem. Eng. J. 387 (2020), 124067, https://doi.org/10.1016/j.cej.2020.124067.
[17] Y. Lin, J. Hu, L. Wu, Q. Zou, D. Chen, D. Huang, H. Lu, S.-B. Wang, H. Zhu, Multiple emission bands NIR-persistent luminescence mSiO2@Zn0.6Ca0.4Ga2O4: Cr3+, Yb3+ nanoparticles for biological applications, J. Mater. Chem. B 9 (2021) 1131–1137, https://doi.org/10.1039/D0TB02552F.
[18] A.N. Bashkatov, E.A. Genina, V.I. Kochubey, V.V. Tuchin, Optical properties of human skin, subcutaneous and mucous tissues in the wavelength range from 400 to 2000 nm, J. Phys. d: Appl. Phys. 38 (2005) 2543, https://doi.org/10.1088/0022-3727/38/15/004.
[19] J.V. Frangioni, In vivo near-infrared fluorescence imaging, Curr. Opin. Chem. Biol. 7 (2003) 626–634, https://doi.org/10.1016/j.cbpa.2003.08.007.
[20] J. Wang, Q. Ma, X.-X. Hu, H. Liu, W. Zheng, X. Chen, Q. Yuan, W. Tan, Autofluorescence-free targeted tumor imaging based on luminous nanoparticles with composition-dependent size and persistent luminescence, ACS Nano 11 (2017) 8010–8017, https://doi.org/10.1021/acsnano.7b02643.
[21] B.-M. Liu, X.-X. Guo, L. Huang, R.-F. Zhou, R. Zou, C.-G. Ma, J. Wang, A Super-broadband NIR dual-emitting Mg2SnO4:Cr3+, Ni2+ phosphor for ratiometric phosphor-converted NIR light source applications, Adv. Mater. Technol. 8 (2023) 2201181, https://doi.org/10.1002/admt.202201181.
[22] M. Li, Y. Jin, L. Yuan, B. Wang, H. Wu, Y. Hu, F. Wang, Near-infrared long afterglow in Fe3+-activated Mg2SnO4 for self-sustainable night vision, ACS Appl. Mater. Interfaces 15 (2023) 13186–13194, https://doi.org/10.1021/acsami.3c00673.
[23] K.N. Kim, H.-K. Jung, H.D. Park, D. Kim, High luminance of new green emitting phosphor, Mg_2SnO_4:Mn, J. Lumin. 99 (2002) 169–173, https://doi.org/10.1016/S0022-2313(02)00334-4.
[24] B. Lei, B. Li, X. Wang, W. Li, Green emitting long lasting phosphorescence (LLP) properties of Mg2SnO4:Mn2+ phosphor, J. Lumin. 118 (2006) 173–178, https://doi.org/10.1016/j.jlumin.2005.08.010.
[25] J.-L. Li, J.-P. Shi, C.-C. Wang, P.-H. Li, Z.-F. Yu, H.-W. Zhang, Five-nanometer $ZnSn_2O_4$:Cr, Eu ultra-small nanoparticles as new near infrared-emitting persistent luminescent nanoprobes for cellular and deep tissue imaging at 800 nm, Nanoscale 9 (2017) 8631–8638, https://doi.org/10.1039/C7NR02468A.
[26] X. Zhao, K.-C. Zhao, L.-J. Chen, Y.-S. Liu, J.-L. Liu, X.-P. Yan, A pH reversibly activatable NIR photothermal/photodynamic-in-one agent integrated with renewable nanoimplants for image-guided precision phototherapy, Chem. Sci. 12 (2021) 442–452, https://doi.org/10.1039/D0SC04408C.
[27] B.M. Weckhuysen, H.J. Spooren, R.A. Schoonheydt, A quantitative diffuse reflectance spectroscopy study of chromium-containing zeolites, Zeolites 14 (1994) 450–457, https://doi.org/10.1016/0144-2449(94)90171-6.
[28] M.F.P. Graça, S.P. Miguel, C.S.D. Cabral, I.J. Correia, Hyaluronic acid-based wound dressings: a review, Carbohydr. Polym. 241 (2020), 116364, https://doi.org/10.1016/j.carbpol.2020.116364.
[29] Z. Hussain, M. Pandey, H.E. Thu, T. Kaur, G.W. Jia, P.C. Ying, T.M. Xian, M.A. S. Abourehab, Hyaluronic acid functionalization improves dermal targeting of polymeric nanoparticles for management of burn wounds: In vitro, ex vivo and in vivo evaluations, Biomed. Pharmacother. 150 (2022), 112992, https://doi.org/10.1016/j.biopha.2022.112992.
[30] W. Jiang, L. Huang, F. Mo, Y. Zhong, L. Xu, F. Fu, Persistent luminescent multifunctional drug delivery nano-platform based on nanomaterial ZnGa2O4:Cr3+, Sn4+ for imaging-guided cancer chemotherapy, J. Mater. Chem. B 7 (2019) 3019–3026, https://doi.org/10.1039/C9TB00109C.
[31] T. Shi, W. Sun, R. Qin, D. Li, Y. Feng, L. Chen, G. Liu, X. Chen, H. Chen, X-ray-induced persistent luminescence promotes ultrasensitive imaging and effective inhibition of orthotopic hepatic tumors, Advanced Functional Materials 30 (24) (2020) 2001166, https://doi.org/10.1002/adfm.202001166.
[32] B. Yu, Y.-J. Wang, Y.-Y. Lin, Y. Feng, J. Wu, W.-S. Liu, M. Wang, X.-P. Gao, HKUST-1 nano metal–organic frameworks combined with ZnGa2O4:Cr3+ near-infrared persistent luminescence nanoparticles for in vivo imaging and tumor chemodynamic and photothermal synergic therapy, Nanoscale 14 (25) (2022) 8978–8985, https://doi.org/10.1039/D1NR07927A.
[33] L. Umaralikhan, M. Jamal Mohamed Jaffar, Green synthesis of MgO nanoparticles and its antibacterial activity, Iran. J. Sci. Technol. 42 (2018) 477–485, https://doi.org/10.1007/s40995-016-0041-8.
[34] H. Tang, C. Cheng, G. Yu, H. Liu, W. Chen, Structure and electrochemical properties of Mg_2SnO_4 nanoparticles synthesized by a facile co-precipitation method, Mater. Chem. Phys. 159 (2015) 167–172, https://doi.org/10.1016/j.matchemphys.2015.03.066.
[35] L. Jinlei, G. Jiaqing, L. Hao, Q. Junle, S. Jun, Simultaneous realization of persistent luminescence and CT dual-mode imaging by x-ray recharged Bi2Ga4O9: Cr nanoprobes in depth-independent tumors, Chem. Eng. J. 406 (2021), 126008, https://doi.org/10.1016/j.cej.2020.126008.
[36] A. Pandey, K. Singh, S. Patel, R. Singh, K. Patel, K. Sawant, Hyaluronic acid tethered pH-responsive alloy-drug nanoconjugates for multimodal therapy of glioblastoma: An intranasal route approach, Mater. Sci. Eng. C 98 (2019) 419–436, https://doi.org/10.1016/j.msec.2018.12.139.
[37] S. Wang, J.Z. Cai, R. Pang, H.Y. Wu, Y.Q. Luo, T. Tan, W.H. Yuan, L.H. Jiang, C. Y. Li, H.J. Zhang, Synthesis and luminescence properties of a broadband near-infrared emitting non-gallate persistent luminescence Mg1.4Zn0.6SnO4:Cr3+ phosphor, Dalton Trans. 50 (2021) 5666–5675, https://doi.org/10.1039/d1dt00452b.
[38] W. Xie, W. Jiang, R. Zhou, J. Li, J. Ding, H. Ni, Q. Zhang, Q. Tang, J.-X. Meng, L. Lin, Disorder-induced broadband near-infrared persistent and photostimulated luminescence in Mg_2SnO_4:Cr^3+, Inorg. Chem. 60 (2021) 2219–2227, https://doi.org/10.1021/acs.inorgchem.0c02941.
[39] B.-B. Wang, L.-X. Yan, L.-J. Chen, X. Zhao, X.-P. Yan, Responsive nanoplatform for persistent luminescence “turn-on” imaging and “on-demand” synergistic therapy of bacterial infection, J. Colloid Interf. Sci 610 (2022) 687–697, https://doi.org/10.1016/j.jcis.2021.11.125.
[40] L.-X. Yan, B.-B. Wang, X. Zhao, L.-J. Chen, X.-P. Yan, A pH-responsive persistent luminescence nanozyme for selective imaging and killing of helicobacter pylori and common resistant bacteria, ACS Appl. Mater. Interfaces 13 (2021) 60955–60965, https://doi.org/10.1021/acsami.1c21318.
[41] Y.-B. Su, X. Zhao, L.-J. Chen, H.-L. Qian, X.-P. Yan, 6-Triphenylphosphinehexanoic acid conjugated near-infrared persistent luminescence nanoprobe for autofluorescence-free targeted imaging of mitochondria in cancer cells, ChemNanoMat 6 (2020) 427–434, https://doi.org/10.1002/cnma.201900697.